Towards Atomic-Scale Control over Structural Modulations in Quasi-1D Chalcogenides for Colossal Optical Anisotropy

Guodong Ren[1*#], Shantanu Singh[2,3#], Gwan Yeong Jung[4#], Wooseon Choi[5], Huandong Chen[2], Boyang Zhao[2], Kevin Ye[2], Andrew R. Lupini[6], Miaofang Chi[6], Jordan A. Hachtel[6], Young-Min Kim[5,7], Jayakanth Ravichandran[2,3,8*], Rohan Mishra[1,4*]

[1] *Institute of Materials Science and Engineering, Washington University in St. Louis, St. Louis, MO 63130, USA*

[2] *Mork Family Department of Chemical Engineering and Materials Science, University of Southern California, Los Angeles, CA 90089, USA*

[3] *Core Center of Excellence in Nano Imaging, University of Southern California, Los Angeles, CA 90089, USA*

[4] *Department of Mechanical Engineering and Material Science, Washington University in St. Louis, St. Louis, MO 63130, USA*

[5] *Department of Energy Science, Sungkyunkwan University, Suwon 16419, Republic of Korea*

[6] *Center for Nanophase Materials Sciences, Oak Ridge National Laboratory, Oak Ridge, TN 37830, USA*

[7] *Center for 2D Quantum Heterostructures, Institute for Basic Science, Suwon 16419, Republic of Korea*

[8] *Ming Hsieh Department of Electrical Engineering, University of Southern California, Los Angeles, CA 90089, USA*

[#]These authors contributed equally: Guodong Ren, Shantanu Singh, Gwan Yeong Jung

*Corresponding authors: Guodong Ren (guodong.ren@wustl.edu); Jayakanth Ravichandran (j.ravichandran@usc.edu); Rohan Mishra (rmishra@wustl.edu)

Keywords: Quasi-1D chalcogenide, structural modulations, refractive index, charge ordering, optical anisotropy, electron microscopy

ABSTRACT

Optically anisotropic materials are sought after for tailoring the polarization of light. Recently, colossal optical anisotropy ($\Delta n = 2.1$) was reported in a quasi-one-dimensional chalcogenide, $Sr_{9/8}TiS_3$. Compared to $SrTiS_3$, the excess Sr in $Sr_{9/8}TiS_3$ leads to periodic structural modulations and introduces additional electrons — that undergo charge ordering on select Ti atoms to form a highly polarizable cloud oriented along the *c*-axis, hence, resulting in the colossal optical anisotropy. Here, further enhancement of the colossal optical anisotropy to $\Delta n = 2.5$ in $Sr_{8/7}TiS_3$ is reported through control over the periodicity of the atomic-scale modulations. The role of structural modulations in tuning the optical properties in a series of Sr_xTiS_3 compounds with $x = [1, 9/8, 8/7, 6/5, 5/4, 4/3, 3/2]$ is investigated using density-functional-theory (DFT) calculations. The structural modulations arise from various stacking sequences of face-sharing TiS_6 octahedra and twist-distorted trigonal prisms and are found to be thermodynamically stable for $1<x<1.5$. As x increases, an indirect-to-direct band gap transition is predicted for $x \geq 8/7$ along with an increased occupancy of Ti-d_{z^2} states. Together, these two factors result in a theoretically predicted maximum birefringence of $\Delta n = 2.5$ for $Sr_{8/7}TiS_3$. Single crystals of $Sr_{8/7}TiS_3$ were grown using a molten-salt flux method. Single crystal X-ray diffraction measurements confirm the presence of long-range order with a periodicity corresponding to $Sr_{8/7}TiS_3$, which is further corroborated by atomic-scale observations using scanning transmission electron microscopy. Polarization-resolved Fourier-transform infrared spectroscopy of $Sr_{8/7}TiS_3$ crystals shows $\Delta n \approx 2.5$, in excellent agreement with the theoretical predictions. Overall, these findings demonstrate the compositional tunability of optical properties in Sr_xTiS_3 compounds by control over atomic scale modulations, and suggest that similar strategies could be extended to other compounds having modulated structures.

Introduction

Upon passing through a dielectric medium, the optical characteristics of light, including its speed, phase and intensity, are altered by the frequency-dependent complex index of refraction, $(n + i\kappa)$, of the medium, where n is the refractive index and κ is the extinction coefficient. Optically anisotropic materials have different index of refraction along different crystallographic orientations. Their anisotropy is characterized by birefringence (Δn) and dichroism ($\Delta\kappa$), which are, respectively, the difference between the refractive index and the extinction coefficient along two polarization directions[1, 2]. Optically anisotropic materials, particularly those having large and tunable Δn and $\Delta\kappa$, are useful for generating and controlling polarized light, thereby enabling photonic applications through devices such as wave plates[3, 4] and optical sensors[5, 6].

Conventional birefringent crystals, such as calcite[1, 7] and rutile[8], show modest birefringence with $\Delta n < 0.3$ in spectral regions where they have high transparency. Recently, giant birefringence with $\Delta n > 0.5$, has been reported in several lower dimensional materials, including quasi-1D crystals and layered two-dimensional (2D) materials[9, 10]. Layered 2D materials have highly anisotropic bonding with weak interlayer van der Waals bonds and strong covalent intralayer bonds, which results in a large birefringence. h-BN and MoS_2 show $\Delta n \approx 0.7$ and 1.5 within their transparent region, respectively[9, 10]. However, harnessing the birefringence in layered 2D materials is challenging given that their optic axis is perpendicular to the weakly bonded layers. Organic–inorganic hybrid birefringent materials have been found to exhibit large intrinsic polarizability, attributed to the directional arrangement of birefringence-active groups. For instance, $Li_3(C_9N_{13})\cdot 6H_2O$ and $[AgSePh]_\infty$ (Mithrene) demonstrate large birefringence ($\Delta n > 1$) in the short wavelength regime (400–500 nm)[11, 12]. However, the mechanical fragility and poor thermal and environmental stability of organic and hybrid crystals limit their practical application[13]. In these aspects, single crystals of quasi-1D perovskite chalcogenides are attractive. Niu *et al.* reported $\Delta n > 0.7$ in a broadband lossless spectral region spanning from mid- to long-wave infrared in single crystals of $BaTiS_3$.[14] These single crystals are mechanically robust compared to 2D van der Waals materials and possess excellent thermal stability in air at least up to 550 °C[15]. They can also be grown along different orientations using scalable methods,[16, 17] thus providing different surface facets and optical axes with varying refractive index[17-22]. Recently, colossal optical anisotropy with $\Delta n \approx 2.1$ was reported in single crystals of another quasi-1D chalcogenide, $Sr_{9/8}TiS_3$[18]. Both $Sr_{9/8}TiS_3$ and $BaTiS_3$ have similar structures with chains of face-sharing TiS_6 polyhedra running along the long *c*-axis and arranged in a hexagonal pattern in the basal *ab*-plane. The Sr/Ba cations occupy the interchain interstitial positions. Compared to stoichiometric $BaTiS_3$, the excess Sr atoms in $Sr_{9/8}TiS_3$ modulate the TiS_6 chains into alternating blocks of octahedral and trigonal prismatic units with repeating periodicity. Furthermore, the additional electrons introduced by the excess

Sr^{2+} cations selectively localize on Ti atoms lying within the periodic modulations to form electron pockets that are oriented along the *c*-axis. These electron pockets selectively boost the polarizability along the *c*-axis, ultimately giving rise to the colossal birefringence[18]. Hexagonal perovskites, especially oxides, have also been reported to form modulated structures with varying stoichiometry and periodicity[23, 24]. Given the crucial role that the structural modulations play in enhancing the optical anisotropy in $Sr_{9/8}TiS_3$, a natural question that arises is whether the periodicity of the structural modulations and the excess electrons introduced by the Sr non-stoichiometry in Sr_xTiS_3 ($x \geq 1$) affect its optical anisotropy. If they do, then control over the modulation periodicity through synthesis methods[25] can enable access to crystals with varying birefringence.

In this Article, we report a record birefringence of Δn = 2.5 in $Sr_{8/7}TiS_3$ single crystals following computational predictions that show the tunability of optical anisotropy with control over atomic-scale structural modulations in Sr_xTiS_3. We use first-principles density-functional theory (DFT) calculations to investigate the thermodynamic stability and the optical properties of a series of modulated Sr_xTiS_3 structures. The calculations reveal that modulated structures with x=[1, 9/8, 8/7, 6/5, 5/4, 4/3, 3/2] are thermodynamically stable, while x = [1, 3/2] are above the convex hull. As x increases from $SrTiS_3$, additional valence electrons from the Sr^{2+} ions populate the Ti-d_{z^2} states, which are nominally unoccupied in $SrTiS_3$. Two electronic factors are found to affect the optical anisotropy in this system: the direct or indirect nature of the bandgap and the occupancy of the Ti-d_{z^2} states. The birefringence in Sr_xTiS_3 increases from Δn = 2.1 in the indirect bandgap compound $Sr_{9/8}TiS_3$ to a peak value of Δn = 2.5 in $Sr_{8/7}TiS_3$ — that has a direct bandgap —, followed by a monotonic decrease to Δn = 1.2 in $Sr_{4/3}TiS_3$. Subsequently, we report the results of our experimental efforts to control the modulation periodicity in Sr_xTiS_3 by varying the stoichiometry. We employed two distinct synthesis methods to obtain Sr_xTiS_3 single crystals with two different stoichiometries. $Sr_{9/8}TiS_3$ single crystals were obtained using chemical vapor transport with iodine as a transport agent. $Sr_{8/7}TiS_3$ single crystals were grown using molten-salt flux method, with potassium iodide (KI) as the flux. The crystal structures for both compositions were determined using single crystal X-ray diffraction (SC-XRD) measurements. Using aberration-corrected scanning transmission electron microscopy (STEM), we directly resolve the atomic structure and the modulation periodicity in $Sr_{9/8}TiS_3$ and $Sr_{8/7}TiS_3$ single crystals, respectively. Using Fourier-transform infrared spectroscopy (FTIR), we measured a record birefringence for $Sr_{8/7}TiS_3$, in excellent agreement with the DFT predictions. These findings highlight control over atomic-scale structural modulations in Sr_xTiS_3 as an effective strategy for tuning its optical anisotropy. Beyond establishing a new record birefringence in $Sr_{8/7}TiS_3$, our research underscores the untapped potential of modulated hexagonal perovskites — a vast and underexplored materials space — for achieving anisotropic physical properties.

Results and Discussion

Structural modulations in Sr_xTiS_3

With a chemical formula of $A_xMX'_3$ (A = alkaline metal, M = transition metal, X' = anion), hexagonal perovskites form a series of structures having infinite chains of face-sharing MX'_6 polyhedra that are stacked in a hexagonal manner and are separated by the A-site cations. The MX'_6 polyhedral chains can modulate between octahedral and trigonal prismatic units with the periodicity of the modulations being either commensurate or incommensurate[23, 24, 26-28]. Sr_xTiS_3 compounds ($x > 1$) have been reported to be predominantly off-stoichiometric with $Sr_{9/8}TiS_3$ and $Sr_{8/7}TiS_3$ as the commonly observed modulations.[18, 29, 30]. These modulated Sr_xTiS_3 structures can be described as stacks of face-sharing TiS_6 octahedra (O), shown in blue in Figure 1a, and distorted trigonal prisms (T), shown in red. The arrangement and the ratio of these two building blocks are contingent upon the value of x.

Besides the experimentally reported modulated structures $Sr_{9/8}TiS_3$ and $Sr_{8/7}TiS_3$[18, 29, 30], we also constructed the following modulation periodicities based on their isostructural oxide counterparts: $Sr_{6/5}TiS_3$ ($Sr_{6/5}CoO_3$[31]), $Sr_{5/4}TiS_3$ ($Sr_{5/4}CoO_3$[32]), $Sr_{4/3}TiS_3$ ($Sr_{4/3}NiO_3$[33]), and $Sr_{3/2}TiS_3$ ($Sr_{3/2}CoO_3$[34]). We optimized all the structures using DFT and assigned space groups to the optimized structures using the ISOTROPY Software Suite[35]. It is important to note that stoichiometric $SrTiS_3$ has not been experimentally realized. Similar to previous work[18], in our theoretical calculations, we have used a hypothetical stoichiometric $P2_1$-$SrTiS_3$ structure derived by freezing the soft phonon modes with imaginary frequencies present in the high-symmetry $P6_3/mmc$-$SrTiS_3$ phase. Compared to stoichiometric $SrTiS_3$, the modulated Sr_xTiS_3 compounds have the Sr atoms displaced along the ab-plane and are accompanied by a twist distortion of TiS_6 units from octahedral to trigonal-prismatic configuration. The stacking sequence of the polyhedral building blocks (classified as O and T) defines the modulation periodicity of the Sr_xTiS_3 compounds. For instance, $Sr_{9/8}TiS_3$ has periodic $[-(T-O-T)-(O)_5-]_2$ repetition of 16 TiS_6 units within every 18 Sr layers along the c-axis, while $Sr_{6/5}TiS_3$ features 5 TiS_6 units with $[-(T)_2-(O)_3-]$ configuration repeating within every 6 Sr layers. For $Sr_{8/7}TiS_3$, the crystal structure was previously refined using the superspace group of $P\bar{3}$ (ICSD-94550), which consists of two distinct stacking sequences, $[-(T-O-T)-(O)_4-]$ and $[-(O)_5-(T)_2-]$ blocks, each containing 7 TiS_6 units[36]. The $P\bar{3}$-$Sr_{8/7}TiS_3$ preserves inversion symmetry along the c-axis by ascribing partial occupancy (0.5) of sulfur atoms at the 6g Wyckoff site. Overall, the superspace group model describes the average symmetry of the global structure with modulation periodicity along c-axis. However, in DFT modeling, we must use either full or zero occupancy for sulfur atoms, as partial occupancy would require further increase in the size of the supercells — that are already large to accommodate the modulations —, making them computationally prohibitive. In this case, definite occupancy of S atoms at

the 6*g* site leads to two structural variants, both consistent with the lower-symmetry *P*3 space group, as shown in Figure 1a, without changing the stacking sequences of TiS_6 units along the *c*-axis as compared with the $P\bar{3}$ structure. Thus, we used a lower-symmetry *P*3-$Sr_{8/7}TiS_3$ model for the theoretical calculations.

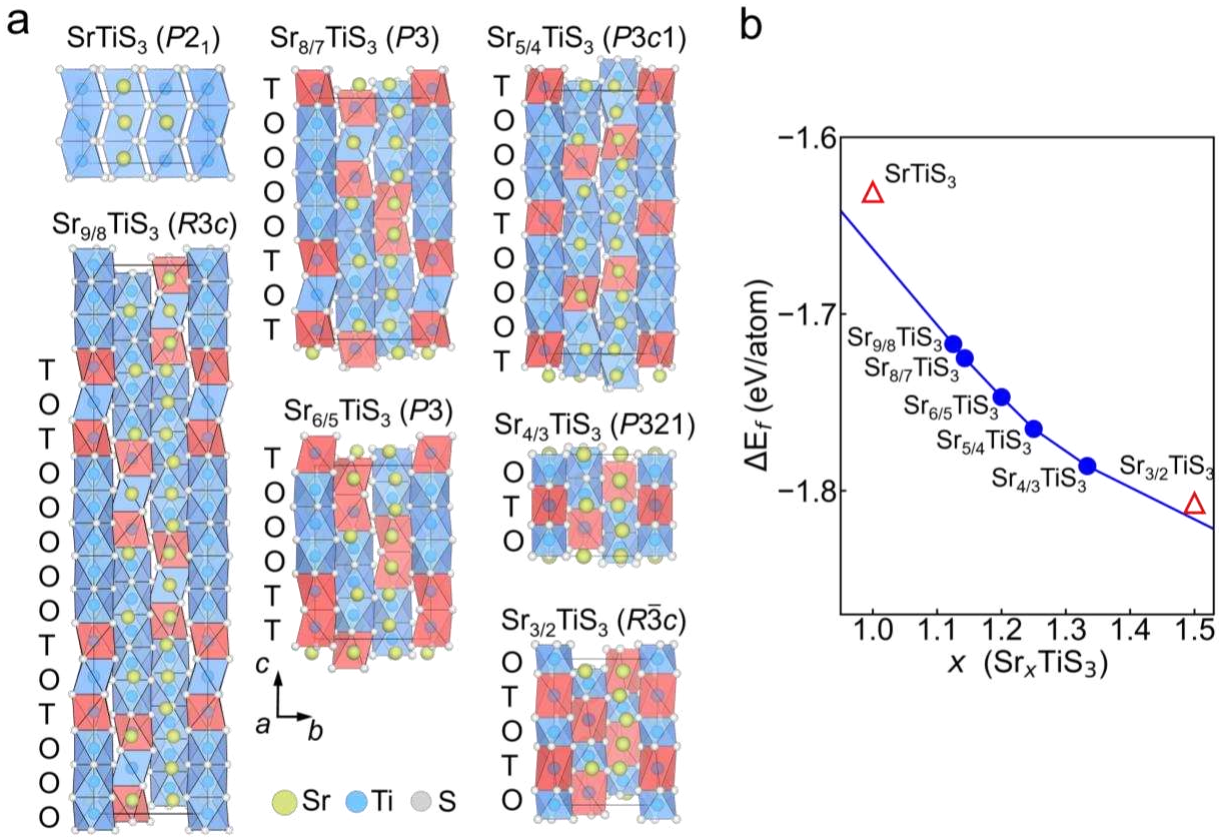

Figure 1. Schematics of modulated Sr_xTiS_3 structures (*x*=[1, 9/8, 8/7, 6/5, 5/4, 4/3, 3/2]) and their thermodynamical stability. **a,** Modulated structures of Sr_xTiS_3 compounds viewed along the [100] zone axis. The octahedral (O) and distorted trigonal prismatic (T) TiS_6 units are highlighted in blue and red, respectively. **b,** Thermodynamic convex hull diagram for Sr_xTiS_3 as a function of the Sr content, *x*. $SrTiS_3$ and $Sr_{3/2}TiS_3$ are metastable having formation energy above the hull.

Thermodynamic stability of Sr_xTiS_3 compounds

To assess the thermodynamic stability of the Sr_xTiS_3 compounds, we constructed the convex hull with respect to the formation energy, ΔE_f, of their possible decomposition products (see details in *Supporting Information Section II*). When a phase has a formation energy above the hull, it is considered metastable, as the system can lower its energy by decomposing into products that lie on the hull. We calculated the DFT total energy (E_{total}) of the Sr_xTiS_3 compounds and all the thermodynamically stable decomposition products, as listed in Table S1. The convex hull was then constructed through the grand canonical linear programming (GCLP) method[37] to identify the decomposition products that minimize the total energy.

From the convex hull results shown in Figure 1b, modulated Sr_xTiS_3 structures with $1< x <1.5$ are thermodynamically stable, while $SrTiS_3$ (x = 1) and $Sr_{3/2}TiS_3$ (x = 1.5) are metastable having formation energy above the hull. Our thermodynamic stability analyses suggest that the modulation periodicity may be changed by growing Sr_xTiS_3 compounds with stoichiometry between $1< x <1.5$. One should also note that, due to the poor scaling of DFT calculations with system size, Sr_xTiS_3 structures having commensurate modulation periodicity (with finite unit cells) were only considered. The existence of incommensurate Sr_xTiS_3 structures with infinitely large unit cells, cannot be excluded. In fact, at high synthesis temperatures, the incommensurate structures are expected to be further stabilized by their higher configurational entropy.

Optical anisotropy of Sr_xTiS_3 compounds

To reveal the changes in optical properties with the structural modulations in Sr_xTiS_3 compounds discussed above, we calculated the frequency (ω)-dependent dielectric function, $\varepsilon_{\parallel/\perp}(\omega) = \varepsilon_{1\parallel/\perp}(\omega) + i\varepsilon_{2\parallel/\perp}(\omega)$, for electric fields along the c-axis ($\parallel$) and perpendicular to it ($\perp$) using the formulation proposed by Gajdoš et al.[38] Using the computed dielectric function, we calculated the refractive index, $n(\omega) = \frac{\sqrt{2}}{2}\left[\sqrt{\varepsilon_1(\omega)^2+\varepsilon_2(\omega)^2}+\varepsilon_1(\omega)\right]^{1/2}$, and the extinction coefficient, $k(\omega) = \frac{\sqrt{2}}{2}\left[\sqrt{\varepsilon_1(\omega)^2+\varepsilon_2(\omega)^2}-\varepsilon_1(\omega)\right]^{1/2}$. The calculated optical properties of all the Sr_xTiS_3 compounds, excluding $Sr_{3/2}TiS_3$ which is computed to be metallic, are shown in Figure 2 and Figure S2 (*Supporting Information Section III*). From these plots, it is evident that the modulation periodicity in Sr_xTiS_3 has a significant effect on the dielectric response along the c-axis, as depicted by $n_\parallel(\omega)$ in Figure 2b, and $k_\parallel(\omega)$ in Figure 2e. In contrast, these modulations have a minimal impact on the ab-plane dielectric response, as shown in Figure 2a [$n_\perp(\omega)$], and Figure 2d [$k_\perp(\omega)$]. As the value of x increases in Sr_xTiS_3, the refractive index along the c-axis, $n_\parallel(\omega)$, first increases from 4.83 (x = 9/8) to 5.40 (x = 8/7), then decreases monotonically to 3.70 (x = 4/3) within the lossless spectral region (6 to 16 μm). In contrast, the ab-plane refractive index, $n_\perp(\omega)$, remains relatively constant. This selective change of refractive index along the c-axis results in a change in the optical anisotropy with the modulation periodicity in these Sr_xTiS_3 compounds. Specifically, we find Δn of Sr_xTiS_3 varies from 2.1 to 1.2 in the lossless spectral region with increasing x, as shown in Figure 2c. A similar trend is also observed for the linear dichroism ($\Delta\kappa$) of Sr_xTiS_3. With increasing Sr content, the extinction coefficient along the c-axis, $k_\parallel(\omega)$, shows a significant reduction, dropping from 3.97 at x = 9/8 to 1.38 at x = 4/3 within the spectral region of 1 to 4 μm. In contrast, the extinction coefficient along the ab-plane, $k_\perp(\omega)$, remains nearly unchanged around 0. This pronounced decrease in $k_\parallel(\omega)$, coupled with the constant value of $k_\perp(\omega)$, leads to a corresponding reduction in $\Delta\kappa$ from 3.86 to 1.37 with increasing x in Sr_xTiS_3, as shown in Figure 2f.

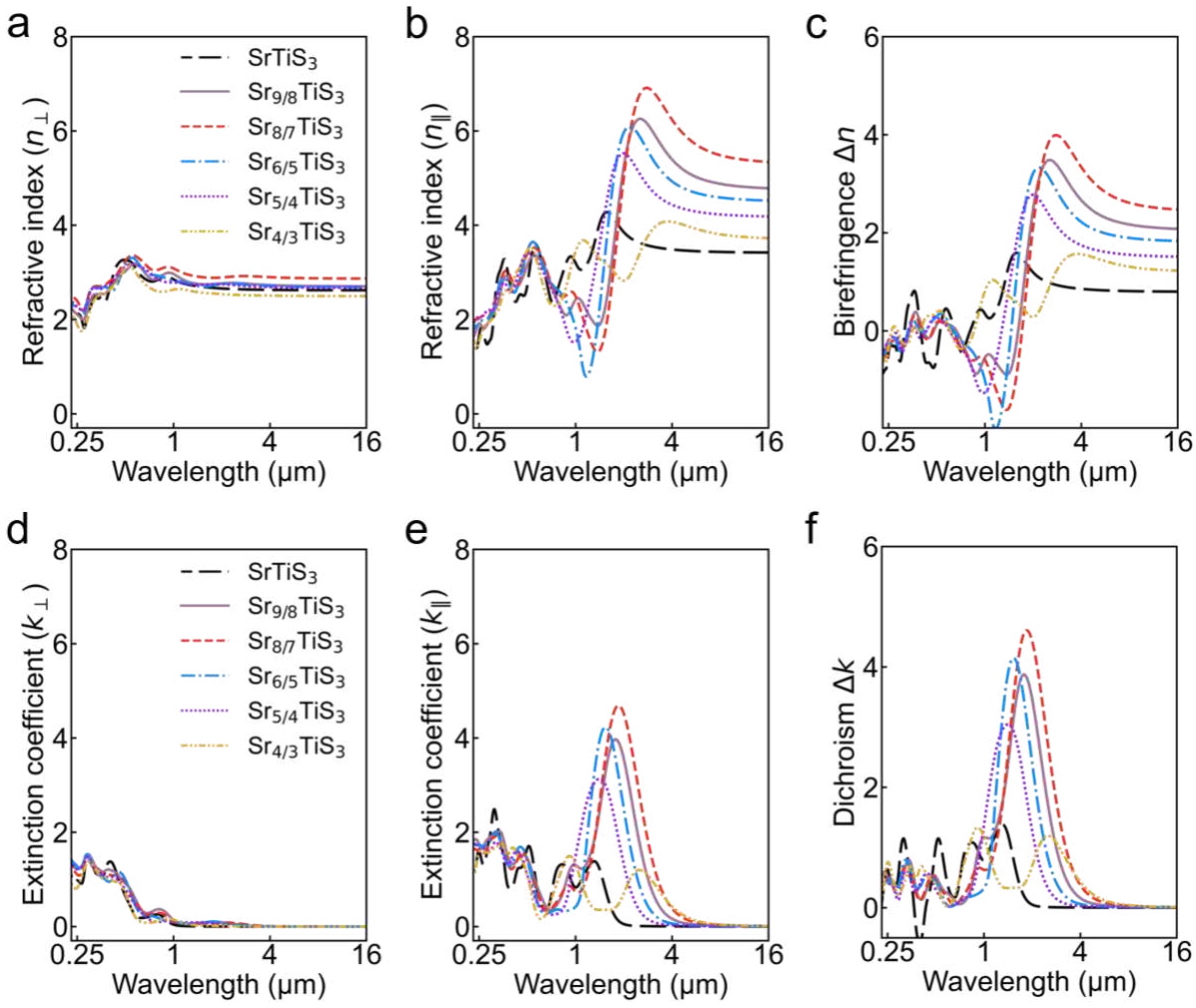

Figure 2. DFT-calculated optical properties of modulated Sr_xTiS_3 compounds (*x*=[1, 9/8, 8/7, 6/5, 5/4, 4/3]). a-b, Calculated refractive indices of the Sr_xTiS_3 compounds for electric polarization along the *ab*-plane $[n_\perp(\omega)]$ in **a** and along the *c*-axis $[n_\parallel(\omega)]$ in **b**. **c**, Comparison of birefringence (Δn) of the Sr_xTiS_3 compounds considering the extraordinary direction parallel to the *c*-axis. **d-e**, Calculated extinction coefficients of the Sr_xTiS_3 compounds for electric polarization along the *ab*-plane $[k_\perp(\omega)]$ in **d** and along the *c*-axis $[k_\parallel(\omega)]$ in **e**. **f**, Comparison of dichroic spectra (Δk) of the Sr_xTiS_3 compounds.

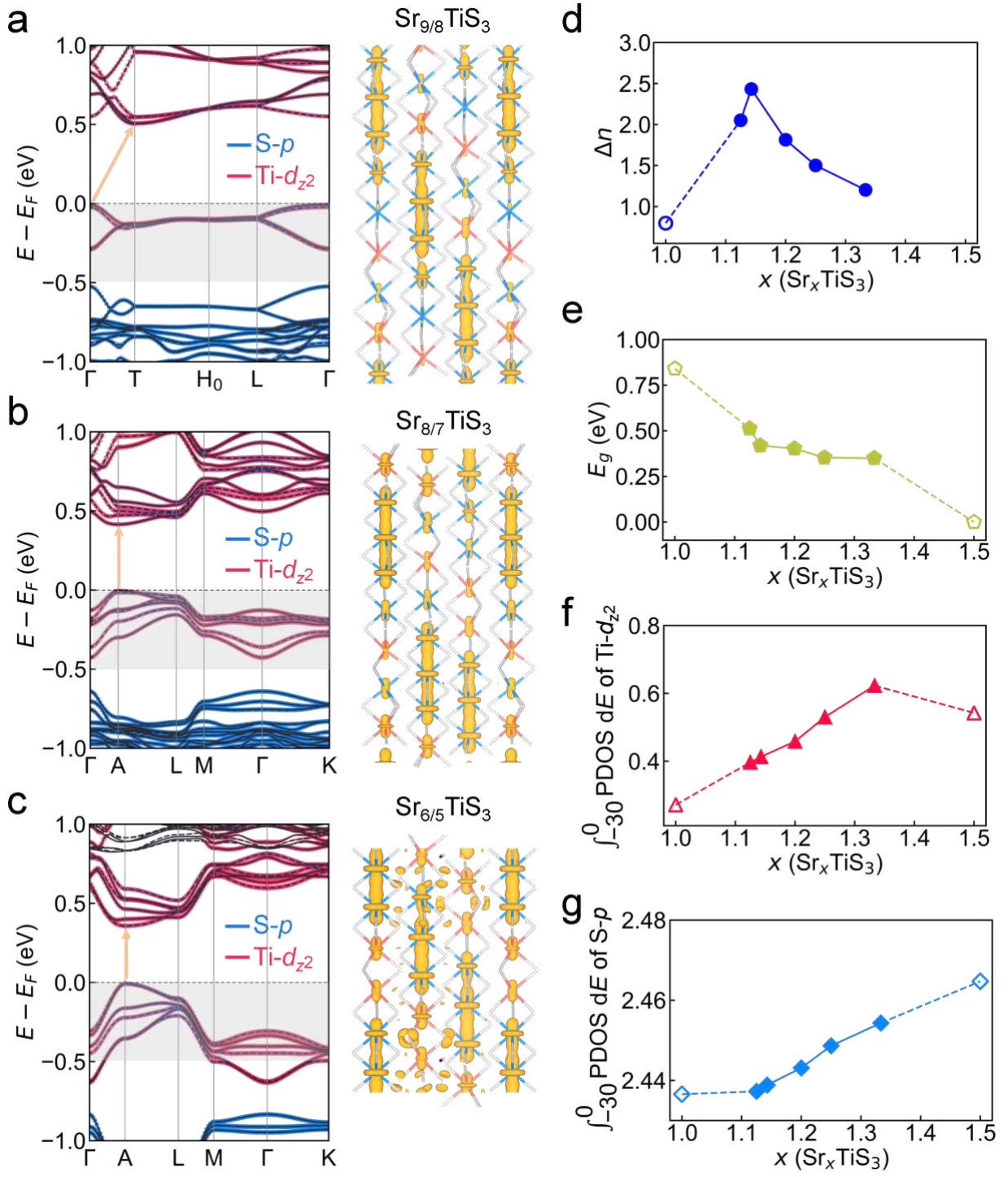

Figure 3. Electronic structures of the Sr_xTiS_3 compounds (x=[9/8, 8/7, 6/5]) having different modulation periodicity. a-c, Left panels: orbital-projected band structures for $Sr_{9/8}TiS_3$ in **a**, $Sr_{8/7}TiS_3$ in **b**, and $Sr_{6/5}TiS_3$ in **c**. The thicker red lines show the contribution from Ti-d_{z^2} states, while the thicker blue lines correspond to S-*p* states. The Fermi energy is set to 0 eV. The orange arrows, connecting the valence band maximum (VBM) to the conduction band minimum (CBM), indicate whether the bandgap is direct or indirect. Right panels: spatial distribution of the valence electrons within 0.5 eV below the Fermi energy

(highlighted with gray boxes in **a-c**). The isosurface is set to an electron density of 0.004 e/Å^3. **d,** Birefringence (Δn) of Sr_xTiS_3 as a function of x. **e,** Bandgap (ΔE_g) of Sr_xTiS_3 as a function of x. **f-g,** Integrated orbital-projected density of Ti-d_{z^2} states in **f** and S-p orbital states in **g** as a function of x. The states were integrated from –30 eV to the Fermi energy at 0 eV. In **d-g**, metastable $Sr_{3/2}TiS_3$ and $SrTiS_3$ are depicted with hollow markers, while the stable compounds are denoted using filled markers.

Electronic structure of Sr_xTiS_3 compounds

The electronic structures of the Sr_xTiS_3 compounds were calculated and analyzed to understand the reason for the variation of Δn with increasing x. Stoichiometric $SrTiS_3$ ($x = 0$) exhibits an indirect bandgap ($\Delta E_g = 0.84$ eV), characterized by a transition between the S-p states in the valence band and the Ti-3d states in the conduction band (as shown in Figure S3 *Supporting Information Section IV*). Stoichiometric $SrTiS_3$ is composed of face-sharing octahedral O units with $D3_d$ point-group symmetry and the Ti–S bonds pointing diagonally along the octahedral coordination. This coordination splits the Ti-3d orbitals into two doublets (e_g^{π} and e_g^{σ}) and a singlet (a_{1g})[39]. The empty Ti-3d states primarily contribute to the conduction bands, with the a_{1g} state, having minimal overlap with the S-p states, being the lowest in energy[18].

In the modulated $Sr_{9/8}TiS_3$ structure, the twist distortion of the TiS_6 octahedra is accompanied by changes in the Ti–Ti spacing along the c-axis from ~2.85 Å at O units (shown as blue in Figure 1a) to ~3.12 Å at the trigonal bipyramidal T units (shown as red in Figure 1a). These structural distortions transform the point group from D_{3d} for the O units to ~D_{3h} at the T units. Additionally, the variations in Ti coordination modify the splitting of the Ti-3d states by lifting their degeneracies at different structural units. As a consequence, the Ti-d_{z^2} states in original TiS_6 O units have been further split into selectively occupied a_{1g} states at O units and empty a_{1g}' states at T units (see the electronic structure and the isosurface plot of charge density in Figure 3a). The energy difference between the occupied a_{1g} states and the empty a_{1g}' states then reforms the bandgap in the modulated $Sr_{9/8}TiS_3$ structures. The character of the edge states in modulated $Sr_{9/8}TiS_3$ is in contrast with stoichiometric $SrTiS_3$ where the band edges are composed of occupied S-p states and empty Ti-d_{z^2} states (See Figure S3). In modulated $Sr_{9/8}TiS_3$, the selectively occupied Ti-d_{z^2} states form a highly oriented electronic blob, exhibiting the strongest dipole transition to the empty Ti-d_{z^2} states along the c-axis, which boosts the electric polarizability along the c-axis ($\varepsilon_{1\parallel}$). As shown in Supplementary Figure S6, the Sr-derived electronic states lie far from the Fermi energy and do not contribute to the band-edge states responsible for the optical transitions.

We observe similar changes in the character of the band edges in other modulated Sr_xTiS_3 compounds, as can be seen in the orbital-projected band structure plots in Figure 3(a-c) (also see Figure S4 in *Supporting*

Information Section IV). Additional electrons from excess Sr atoms preferentially occupy the Ti-d_{z^2} states of the O units. The selective occupation of Ti-d_{z^2} states can be visualized from the isosurface plots of the charge density as depicted in the right panels of Figure 3(a-c). As the ratio of Sr increases (x), more valence electrons from Sr^{2+} ions occupy the Ti-d_{z^2} states hybridized with S-p states — that are mostly unoccupied in $SrTiS_3$. Increasing x also transforms the indirect bandgap in $SrTiS_3$ and $Sr_{9/8}TiS_3$ to a direct bandgap in Sr_xTiS_3 with x=8/7, 6/5, and 5/4. Concurrently, the bandgap decreases monotonically from 0.84 eV in $SrTiS_3$ to 0.35 eV in $Sr_{4/3}TiS_3$, until $Sr_{3/2}TiS_3$ shows metallic character, as shown in Figure 3e. We calculated the occupation of the Ti-d_{z^2} and S-p states by integrating their projected density (see PDOS in Figure S5 in *Supporting Information Section IV*) below the Fermi energy. The results are shown in Figures 3(f-g). We find that with increasing x in Sr_xTiS_3, the occupation of Ti-d_{z^2} and S-p states undergo a noticeable increase to accommodate the additional valence electrons from the excess Sr ions. Overall, the increasing occupation of Ti-d_{z^2} and S-p states is approximately inversely correlated with the decreasing birefringence Δn, as shown in Figure 3d, confirming the critical role of these states in modulating optical anisotropy in Sr_xTiS_3. In modulated $Sr_{9/8}TiS_3$, which has an indirect bandgap, the band-to-band transition strength, as determined by the dipole transition matrix elements[18], reveals that the dipole transitions around the band edge from the selectively occupied Ti-d_{z^2} states to unoccupied Ti-d_{z^2} states lead to a significant enhancement of the dielectric polarizability along the c-axis ($\varepsilon_{1\parallel}$) compared to $SrTiS_3$, where the transitions occur from occupied S-p states to empty Ti-d_{z^2} states (See Figure 2 and Figure S2). Given the similar band-edge characteristics of other modulated Sr_xTiS_3 compounds, it is anticipated that their dielectric functions parallel to the c-axis ($\varepsilon_{1\parallel}$) are also predominantly determined by dipole transitions from the selectively occupied to unoccupied Ti-d_{z^2} states. However, as more Sr ions are introduced in modulated Sr_xTiS_3, two concurrent effects occur. On the one hand, the bandgap evolves from indirect in $SrTiS_3$ and $Sr_{9/8}TiS_3$ to direct with x= 8/7, 6/5 and 5/4, which enhances the direct transitions from valence band to conduction band[40]. On the other hand, the increased Sr content leads to more occupied Ti-d_{z^2} states, thereby reducing the number of available unoccupied Ti-d_{z^2} states in the conduction band. Consequently, the allowed transitions involving Ti-d_{z^2} states along the c-axis are suppressed with increasing x in Sr_xTiS_3. These two critical factors—the nature of the bandgap and the occupancy of the Ti-d_{z^2} states —govern the refractive index $n_{\parallel}(\omega)$ along the c-axis (Figure 2b) and the birefringence Δn. Specifically, $n_{\parallel}(\omega)$ and Δn initially increase when going from $Sr_{9/8}TiS_3$ to $Sr_{8/7}TiS_3$, then decrease monotonically at higher x in Sr_xTiS_3 (Figure 3d). Overall, $Sr_{8/7}TiS_3$ with direct bandgap shows the optimal optical anisotropy as compared to other Sr_xTiS_3 compounds.

Direct observation of structural modulations with varying periodicity in Sr_xTiS_3 crystals

Based on the theoretical calculations, it is evident that $Sr_{9/8}TiS_3$ and $Sr_{8/7}TiS_3$ compositions demonstrate the highest observed optical anisotropy. While Sr_xTiS_3 has been reported to crystallize in powder form through $1.05 \leq x \leq 1.22$ composition range,[41] single crystals have been reported with only two compositions ($Sr_{9/8}TiS_3$[29, 42] and $Sr_{8/7}TiS_3$[36]). Since it is evident from theoretical calculations that $Sr_{9/8}TiS_3$ and $Sr_{8/7}TiS_3$ compositions demonstrate the highest optical anisotropy, we have experimentally explored the potential for controlling the modulation periodicity of Sr_xTiS_3 by employing two distinct growth methods for the two reported stoichiometries. Single crystals of $Sr_{9/8}TiS_3$ were grown using the chemical vapor transport method, as reported elsewhere.[18] We used the molten flux method to obtain the single crystals of $Sr_{8/7}TiS_3$. First, we prepared the precursor powders by the CS_2 sulfurization of commercially available $SrTiO_3$ powders. Then, single crystals of $Sr_{8/7}TiS_3$ were grown using KI as the flux[16] with a 1:40 powder-to-flux ratio. Long, needle-like crystals around a few mm in length and with thickness typically ranging from 25-100 μm were obtained. SC-XRD measurements were performed at 290 K for $Sr_{9/8}TiS_3$ and $Sr_{8/7}TiS_3$ crystals using Mo K-α X-ray radiation. In the case of $Sr_{9/8}TiS_3$, the crystal structure was refined to the trigonal $R3c$ space group, with lattice parameters being $a = b = 11.48$ Å, and $c = 47.75$ Å. For $Sr_{8/7}TiS_3$, the crystal structure was refined to the trigonal space group $P\bar{3}$, with the lattice parameters being $a = b = 11.51$ Å, and $c = 20.95$ Å. These values match well with previously reported values in the literature[18, 36]. To directly observe the structural modulations in the two Sr_xTiS_3 (x= 9/8, 8/7) compounds, we performed atomically resolved imaging using aberration-corrected STEM. High-angle annular dark field (HAADF)-STEM images of the two Sr_xTiS_3 crystals viewed along the [100] zone axis are shown in Figures 4(a-d). In this imaging mode, the intensity of the atomic columns is approximately proportional to the square of the effective atomic number of the columns (Z^2)[43]. When projected along the [100] zone axis, the Ti and Sr columns overlap within −(T−O)− or −(T−T)− building blocks in different modulated Sr_xTiS_3 structures, as shown in Figure S1 (*Supporting Information Section I*). In HAADF-STEM images, these overlapped Ti and Sr columns exhibit higher intensity compared to the Sr-only atomic columns, enabling their distinction based on contrast[18]. This distinctive structural feature is pivotal in our STEM analysis for identifying the structural units and determining the corresponding modulation periodicities in Sr_xTiS_3 compounds.

The $Sr_{9/8}TiS_3$ single crystals display a well-defined modulation periodicity, as demonstrated by the large field-of-view HAADF image in Figure 4a and the corresponding fast Fourier transform (FFT) pattern in the inset. The superlattice spots labeled in the FFT pattern reveal the periodic structural modulation along the c-axis, recurring every 18 atomic layers. This observed modulation periodicity matches our calculated $Sr_{9/8}TiS_3$ structure, as shown in Figure 1a and Figure S1. In the high-magnification HAADF image shown in Figure 4b, we observe a periodic arrangement of brighter triplets, which arise from the overlap of Ti and Sr columns within the triple blocks of –(T–O–T)– along the [100] projection (see Figure S1). By counting the stacking sequence of building blocks (O and T units) from the intensity variations in a line profile, as

shown in Figure 4c, we find that TiS_6 chains have a periodic sequence of $[-(T-O-T)-(O)_5-]_2$ along the *c*-axis. This stacking sequence defines a modulation periodicity of 16 units of TiS_6 within every 18 Sr layers, which further corroborates the modulation periodicity existing in $Sr_{9/8}TiS_3$.

The $Sr_{8/7}TiS_3$ crystals also display a long-range modulation periodicity in the HAADF image (Figure 4c), with the FFT pattern (inset) showing superlattice spots that indicate a structural modulation along the *c*-axis. In the high-magnification HAADF image shown in Figure 4d, we observe two distinct stacking sequences involving $[-(T-O-T)-(O)_4-]$ and $[-(O)_5-(T)_2-]$ blocks, with each block containing 7 TiS_6 units. This structural modulation agrees well with our calculated $Sr_{8/7}TiS_3$ structure (Figure 1a and Figure S1). Furthermore, a detailed comparison of the intensity and spacing between atomic columns in both the experimental and simulated HAADF images, as evidenced by the line profiles in Figure 4d, further validates the local modulation periodicities in $Sr_{8/7}TiS_3$. We also noted that some local regions of the synthesized $Sr_{8/7}TiS_3$ crystals exhibit aperiodic structural modulations, characterized by brighter horizontal columns (perpendicular to the *c*-axis) that segment the crystal into distinct domains, as shown in HAADF-STEM images (Figure S7-S8 in *Supporting Information Section V*). Structural template-matching analyses confirm a mixture of local modulation periodicities of $Sr_{8/7}TiS_3$ and $Sr_{6/5}TiS_3$ in these regions. We must note that, despite the minor, local aperiodicity observed in STEM imaging, our single-crystal diffraction study did not reveal any crystalline inhomogeneity (secondary phases such as $Sr_{6/5}TiS_3$) in the $Sr_{8/7}TiS_3$ crystals, and confirmed that the $Sr_{8/7}TiS_3$ crystals exhibit global, long-range order. The local aperiodicity may arise from the low stacking-fault energy of the $Sr_{8/7}TiS_3$ phase, which is a common characteristic of modulated structures[44-47], and could therefore be intrinsic to the material.

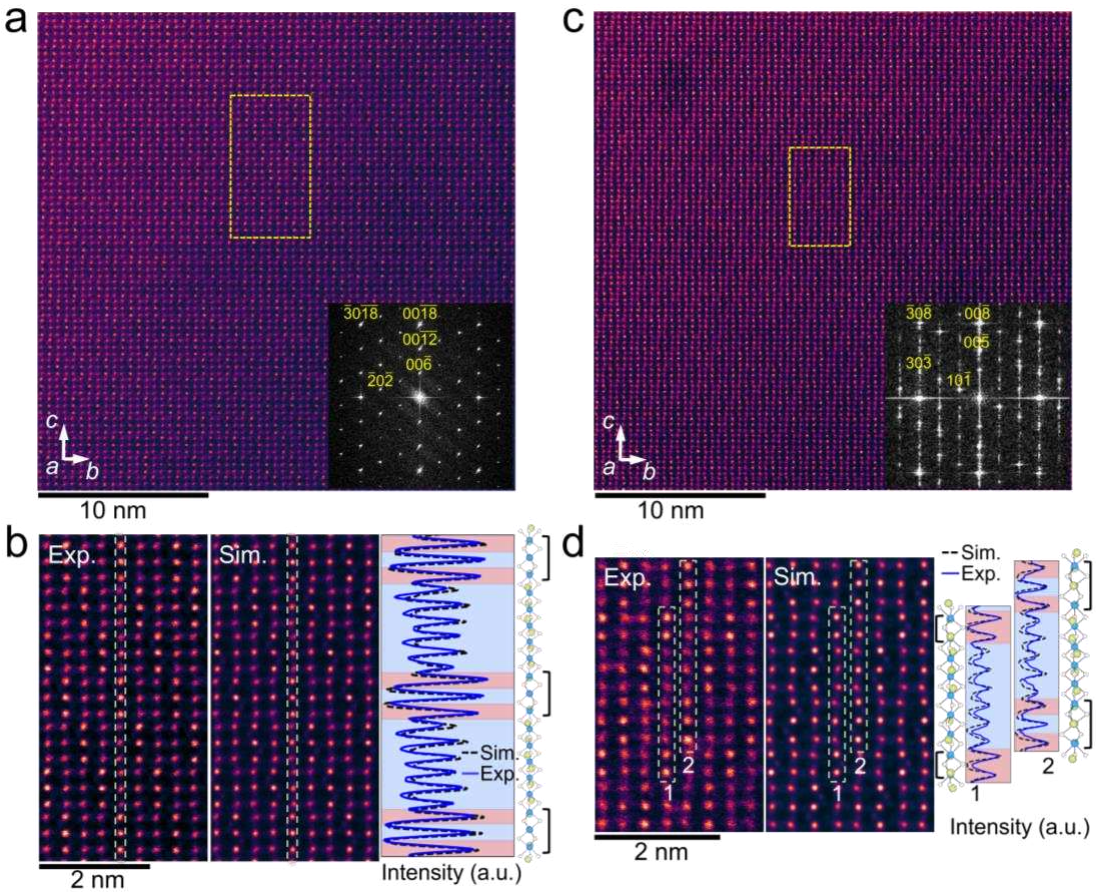

Figure 4. Atomic-resolution HAADF-STEM images of Sr_xTiS_3 crystals with periodic and aperiodic modulations viewed along the [100] axis. a, Large field-of-view HAADF-STEM image of a $Sr_{9/8}TiS_3$ crystal synthesized using chemical vapor transport. The inset shows the corresponding FFT pattern, which matches with the modulation periodicity of $Sr_{9/8}TiS_3$. **b,** High-magnification experimental (leftmost) and simulated (center) HAADF-STEM images of a $Sr_{9/8}TiS_3$ crystal showing the repeating brighter triplets at –(T–O–T)– blocks. In the rightmost panel, the line profile shows the intensity variation across the atomic columns within the yellow dashed box in the HAADF image, where red and blue shaded regions correspond to (T) units and (O) units, respectively. A schematic of one column of atoms within $Sr_{9/8}TiS_3$ is presented on the right where the –(T–O–T)– blocks are highlighted with square brackets. **c,** Large field-of-view HAADF-STEM image of a $Sr_{8/7}TiS_3$ crystal synthesized using molten-flux method. The inset shows the corresponding FFT pattern with superlattice spots indicating the structural modulation along the *c*-axis. **d,** High-magnification experimental (leftmost) and simulated (center) HAADF-STEM images of the yellow dashed box in (c), showing two distinct stacking sequences of brighter doublets and triplets along the *c*-axis: (1) $[-(O)_5-(T)_2-]$ and (2) $[-(T-O-T)-(O)_4-]$ stackings. The rightmost panel displays the intensity variation profiles across the two atomic columns marked by the dashed green boxes in the HAADF images. The (T) and (O) units are indicated with red and blue shaded backgrounds, respectively. Structural schematics of $[-(O)_5-(T)_2-]$ and $[-(T-O-T)-(O)_4-]$ stacking configurations within $Sr_{8/7}TiS_3$ are presented on the right.

Optical anisotropy measurements

To investigate the optical properties of the $Sr_{8/7}TiS_3$ crystals, polarization-resolved FTIR measurements were performed at room temperature in the reflection mode. The polarization of the incident light was kept parallel and perpendicular to the crystal's uniaxial optic axis (c-axis), yielding anisotropic reflectance spectra (Figure 5a). The large optical anisotropy is evident from the significant difference observed in the reflectance for the two polarizations. The reflectance spectra collected for both orientations exhibit Fabry-Pérot interference fringes, originating from the interference between the light reflected from the top and the bottom surface of the measured single-crystal sample. The extinction of the Fabry-Pérot fringes at shorter wavelengths indicates the onset of the absorptive regime. Our DFT calculations demonstrate that the refractive index is relatively constant in the transparent regime. Thus, the periodicity of the interference fringes can be used to approximate the spectrum-averaged real part of the refractive index (n) for the extraordinary ($\parallel c$) and ordinary ($\perp c$) optical directions. The frequency, ν, for such fringes, in case of normal incidence, is related to the refractive index of the material (n) and the thickness of the sample (d), by the relation $\nu = 2nd$.[48, 49] The FFT-derived refractive index values are ~5.1 and ~2.6 for the extraordinary and the ordinary directions, respectively, as shown in Figure 5b, giving a birefringence (Δn) value of ~2.5. To confirm the refractive index values, a two-term Sellmeier equation-based model[50] was used to approximate the wavelength dispersion for the refractive index. The fitting for the model was done to match the periodicity of the fringes observed in the reflectance spectra. The refractive index values from the model match well with the FFT-derived values (*Supporting Information, Section VII*). Figure 5c compares the calculated and experimental birefringence values for Sr_xTiS_3 crystals in the lossless spectral region, showing excellent agreement for both $Sr_{9/8}TiS_3$[18] and $Sr_{8/7}TiS_3$ modulated compounds. Both the theoretical calculations and experimental measurements demonstrate a larger optical anisotropy in $Sr_{8/7}TiS_3$ compared with other modulated Sr_xTiS_3 compounds.

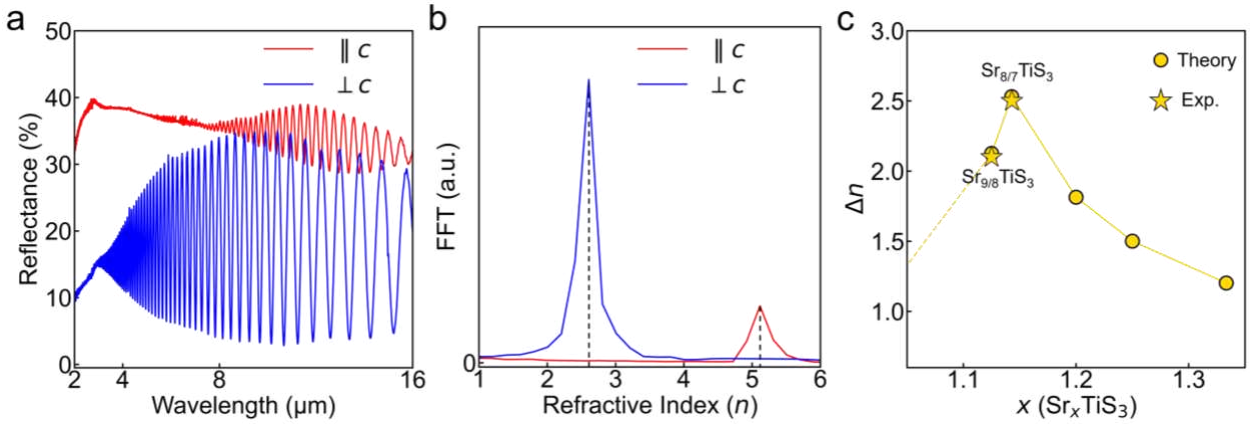

Figure 5. Polarization-resolved FTIR measurements. a, FTIR reflectance spectra for a $Sr_{8/7}TiS_3$ crystal showing large anisotropy between the ordinary (⊥c) and the extraordinary (∥c) polarization. **b,** FFT analysis on the reflectance spectra for the polarization-dependent refractive index of a $Sr_{8/7}TiS_3$ crystal. **c**, Comparison between the experimental and computed birefringence of modulated Sr_xTiS_3 compounds. The birefringence for $Sr_{9/8}TiS_3$ is taken from the literature.[18]

Conclusion

In this work, we have demonstrated that the periodicity of atomic-scale structural modulations in Sr_xTiS_3 structures systematically changes their refractive index and optical anisotropy. DFT calculations suggest that modulated Sr_xTiS_3 structures with $1< x <1.5$ lie on the convex hull, and are expected to be stable against decomposition. With increasing x in modulated Sr_xTiS_3, two concurrent effects occur: first, the bandgap evolves from indirect in $SrTiS_3$ and $Sr_{9/8}TiS_3$ to direct for x=[8/7, 6/5, 5/4], which enhances the direct transitions from the valence band to the conduction band; second, as more Ti-d_{z^2} states become occupied, they result in a reduction of dipole transitions between occupied and empty Ti-d_{z^2} states across the band gap. Together, these two factors—the transformation of the bandgap and the increased occupancy of Ti-d_{z^2} states—determine the refractive index $n_{\parallel}(\omega)$ along the c-axis, and the birefringence Δn. Specifically, $n_{\parallel}(\omega)$ and Δn increase when moving from $Sr_{9/8}TiS_3$ to $Sr_{8/7}TiS_3$, then decrease monotonically for higher x in Sr_xTiS_3. Overall, $Sr_{8/7}TiS_3$ having direct bandgap exhibits the most favorable optical anisotropy ($\Delta n \approx 2.5$) among the Sr_xTiS_3 compounds within the lossless spectral range of 6 to 16 μm. We were able to synthesize $Sr_{9/8}TiS_3$ and $Sr_{8/7}TiS_3$ crystals using two distinct synthesis methods. Direct observation of the atomic structure using STEM imaging, together with SC-XRD measurements establish the structural modulations and confirm long-range order of $Sr_{9/8}TiS_3$ and $Sr_{8/7}TiS_3$. However, $Sr_{8/7}TiS_3$ crystals have local regions showing the presence of stacking faults and minor $Sr_{6/5}TiS_3$ periodicity, highlighting the need to optimize the synthesis conditions for purer structural modulations. Polarization-resolved FTIR measurements confirm the predicted birefringence. By correlating atomic-scale modulations with macroscopic anisotropy, we provide a framework for designing material candidates with variable properties for targeted photonic applications such as optical communication and polarized imaging. The demonstration of record Δn in $Sr_{8/7}TiS_3$ underscores the broader potential of modulation engineering in other hexagonal perovskites,[51] where nanoscale structural complexity can be harnessed to achieve anisotropic optical responses that are inaccessible in conventional crystals. Beyond photonic applications, such atomic-scale modulations may also result in changes in other anisotropic physical properties, involving phonons, and electrons, which are essential for the next-generation electronic and thermoelectric devices.[17]

Methods

Crystal growth

Single crystals of $Sr_{9/8}TiS_3$ were grown via the chemical vapor transport method using iodine as the transport agent. Strontium sulfide powder (Alfa Aesar, 99.9%), titanium powder (Alfa Aesar, 99.9%), sulfur pieces (Alfa Aesar, 99.999%), and iodine pieces (Alfa Aesar 99.99%) were stored and handled in a nitrogen-filled glove box. SrS, Ti, and S in a 1: 1: 2 ratio, with a total weight of 1.0 g, were added to a quartz ampoule along with ~0.75 $mgcm^{-3}$ of iodine. The quartz ampoule was evacuated and sealed using a blow torch. The sealed ampoule was then loaded into a two-zone furnace, where it was heated to the reaction temperature of 1055 °C at 100 °C/h and held for 150 hours before turning off the furnace. The temperature gradient in the dual-zone furnace was kept at 5 °C/cm.

For $Sr_{8/7}TiS_3$, single crystal growth was done in two steps. First, polycrystalline powders of $Sr_{8/7}TiS_3$ were synthesized in a CS_2 annealing setup. Strontium titanate powders (Thermo Fisher, 99%) were loosely packed in an alumina furnace and loaded into a tube furnace. The furnace was heated to 800 °C, using a ramp rate of 10 °C/min, and held for 24 hours. During the reaction, argon was bubbled through CS_2 (Alfa Aesar, 99.9 %) with a flow rate of 12 sccm. After the hold time, the furnace was turned off, and the sample was allowed to cool down naturally. For single crystal growth using KI as flux, 10 g pre-dried KI powder (Alfa Aesar, 99.9%) and 366 mg of $Sr_{8/7}TiS_3$ powder in a 1: 40 powder: flux ratio were added to a quartz ampoule. The quartz ampoule was evacuated and sealed using a blow torch and loaded into a 6" tube furnace in a vertical position. The ampoule was heated to 1050 °C in 20 hours and held at that temperature for 20 hours, followed by a slow down to 650 °C using a ramp rate of 1 °C/hour. After that, the furnace was turned off. The single crystals were obtained by washing off the flux with cold, deionized water.

DFT calculations

Density-functional theory (DFT) calculations were performed using projector augmented-wave potentials[52] as implemented in the Vienna Ab initio Simulation Package (VASP)[53, 54]. The Perdew-Burke-Ernzerhof (PBE) functional within the generalized gradient approximation (GGA)[55] was used to describe the exchange-correlation interactions. A plane-wave basis set with an energy cutoff of 600 eV and 10^{-8} eV for the electronic convergence were applied. A *k*-point spacing of 0.025 $Å^{-1}$ was chosen for both the structure optimization and total-energy calculations. The crystal structures were optimized until all forces on the atoms were less than 10^{-4} eV/Å. To better describe the localization of Ti-*d* electrons, we used the DFT + *U* approach[56]. An effective on-site Hubbard $U = 3.0$ eV was used for the Ti-*d* electrons based on a previous study[18]. Furthermore, we considered magnetic configurations for all the modulated Sr_xTiS_3 structures. The special quasi-random structure (SQS) model implemented in the alloy theoretic automatic toolkit[57, 58] was used to generate best approximations of randomness in the paramagnetic configuration. The

visualization of band-decomposed charge density was performed for valence electrons within 0.5 eV below the Fermi energy. The frequency-dependent dielectric function was calculated by with the LOPTICS tag in the independent particle approximation (IPA)[38] as implemented within VASP. Convergence tests for the number of empty conduction band states were performed based on a previous study[18]. Considering the calculation efficiency and accuracy, we set the total number of energy bands to be 2.5 times as many as the number of valence bands for the dielectric function calculations.

Structural characterization

Single crystal XRD measurements were done using a Rigaku XtaLAB Synergy-S diffractometer equipped with dual source (Cu and Mo, PhotonJet-S) and a HyPix-6000HE detector, using Mo Kα radiation (0.7107 Å) with a power setting of 50 kV and 1 mA. The diffractometer was equipped with an Oxford Cryosystems Cryostream 800, which was used for low-temperature measurements. Crystals were mounted on MiTeGen Kapton loops (Dual Thickness MicroMountsTM) and placed on the goniometer head. Data reduction and scaling were done in CrysAlisPro, and crystal structures were solved and refined in ShelXle.

STEM characterization

We prepared [100]-oriented TEM specimens from two Sr_xTiS_3 crystals using Ar-ion milling. The specimen thinning process involved utilizing a 4 keV ion beam with an angle of incidence at 5°, followed by a 1 keV ion beam with an angle of incidence at 2°. Scanning transmission electron microscope (STEM) imaging was performed using an aberration-corrected Nion UltraSTEM 100 operated at 100 kV with a nominal convergence semi-angle of 30 mrad. HAADF images were acquired using an annular dark-field detector with inner and outer collection semi-angles of 80 and 200 mrad, respectively. To improve the signal-to-noise ratio and correct the image drift, we recorded a sequence of 20 HAADF images with fast scan (dwell time of 1 μs), to enable post-processing correction of sample drift and image registration.

Energy-dispersive X-ray spectroscopy (EDS) imaging in STEM mode was performed using a double-silicon drift detector (JED-2300T, Jeol Ltd.) equipped in a STEM instrument (ARM200CF, Jeol Ltd.). Each EDS detector has an effective X-ray sensing area of 100 mm^2 and provides a large effective solid angle of ~1.2 sr, which guarantees ~10% collection efficiency for the generated X-ray signals (4π sr).

To interpret the intensity variation in the STEM images, multi-slice simulations were carried out on the structures of Sr_xTiS_3. The structures of Sr_xTiS_3 were obtained after structural optimization using DFT. STEM-HAADF simulations were performed using the multi-slice method as implemented in μSTEM[59]. The sample thickness was set to 15 nm and the defocus value was set to 10 Å to obtain good agreement in intensity profiles with the experimental data. We performed the simulations using an aberration-free probe

with an accelerating voltage of 100 kV and a convergence semi-angle of 30 mrad. The inner and outer collection angles for the HAADF detector were set to 80 and 200 mrad, respectively.

Fourier Transform Infrared Spectroscopy (FTIR)

Infrared spectroscopy was performed using a Fourier-transform infrared spectrometer (Bruker Vertex 70) connected to an infrared microscope (Hyperion 2000), using a Globar source, a potassium bromide beam splitter, and a mercury-cadmium-telluride (MCT) detector. The single crystal sample was suspended in air for the measurement. A ZnSe holographic wire grid polarizer was used for controlling the polarization of the incident light. Normal incidence reflection measurements were taken using a 15× Cassegrain microscope objective (numerical aperture = 0.4). A gold mirror was used for background measurement. Reflection spectra modelling details can be found in *Supporting Information, Section VII*.

Supporting Information

The Supporting Information is available online:

Details of computational and experimental analyses including: a discussion of Sr_xTiS_3 compounds having varying modulation periodicity, their thermodynamic stability through convex-hull analysis, theoretically predicted complex dielectric function, computed electronic structures, STEM results and analysis showing the presence of stacking faults in $Sr_{8/7}TiS_3$ crystals, Fourier Transform Infrared Spectroscopy (FTIR) of $Sr_{8/7}TiS_3$ crystals, modeling of the experimental refractive index based on the Sellmeier equation, details of single crystal diffraction data collection, data reduction, and structure refinement.

ACKNOWLEDGEMENTS

This work was supported by the National Science Foundation (NSF) through grants DMR-2122070 (G.Y.J., R.M.), 2122071, and 2145797 (G.R., R.M.). The crystal growth and processing capabilities used were supported in part by ONR grant with award number N00014-23-1-2818, and the polarization-resolved spectroscopy studies and tools were supported in part by Army Research Office grants with grant nos. W911NF-24-1-0164 and W911NF-25-1-0022, respectively. Scanning transmission electron microscopy was supported by the Center for Nanophase Materials Sciences (CNMS), which is a US Department of Energy, Office of Science User Facility at Oak Ridge National Laboratory. This work used computational resources through allocation DMR160007 from the Advanced Cyberinfrastructure Coordination Ecosystem: Services & Support (ACCESS) program, which is supported by NSF grants # 2138259, #2138286, #2138307, #2137603, and #2138296. Y.-M.K. acknowledges the support of the National Research Foundation of Korea (NRF) grant (RS-2023-NR076943) funded by the Korean government in

Korea. An NSF grant with award number CHE-2018740 provided funds to acquire the Rigaku XtaLAB Synergy-S diffractometer that was used for single-crystal XRD studies.

Author contributions

G.R. and R.M. conceived the idea and designed the experiments. G.R. performed the theoretical calculations with assistance from G.Y.J. and R.M. S.S., H.C., B.Z. and J.R. synthesized the single crystals of Sr_xTiS_3. S.S., B.Z. and J.R. performed the structural characterization measurements. G.R. carried out STEM experiments and their analyses under the supervision of A.R.L., J.A.H., M.C., and R.M. W.C. and Y.M.K. performed EDS-STEM measurements. S.S., K.Y. and J.R. performed FTIR measurements. G.R. and R.M. drafted the manuscript with edits from all the coauthors.

Competing interests

The authors declare no conflict of interest.

REFERENCES

(1) Bragg, W. L. The refractive indices of calcite and aragonite. *Proceedings of the Royal Society of London. Series A, Containing Papers of a Mathematical and Physical Character* **1924**, *105* (732), 370-386.

(2) Isherwood, B.; James, J. Structural dependence of the optical birefringence of crystals with calcite and aragonite type structures. *Acta Crystallographica Section A: Crystal Physics, Diffraction, Theoretical and General Crystallography* **1976**, *32* (2), 340-341.

(3) Weber, M. F.; Stover, C. A.; Gilbert, L. R.; Nevitt, T. J.; Ouderkirk, A. J. Giant birefringent optics in multilayer polymer mirrors. *Science* **2000**, *287* (5462), 2451-2456.

(4) Oka, K.; Kaneko, T. Compact complete imaging polarimeter using birefringent wedge prisms. *Optics express* **2003**, *11* (13), 1510-1519.

(5) Hlubina, P.; Ciprian, D.; Knyblová, L. Interference of white light in tandem configuration of birefringent crystal and sensing birefringent fiber. *Optics Communications* **2006**, *260* (2), 535-541. DOI: https://doi.org/10.1016/j.optcom.2005.10.078.

(6) Liu, Y.; Liu, B.; Feng, X.; Zhang, W.; Zhou, G.; Yuan, S.; Kai, G.; Dong, X. High-birefringence fiber loop mirrors and their applications as sensors. *Applied optics* **2005**, *44* (12), 2382-2390.

(7) Maslen, E.; Streltsov, V.; Streltsova, N.; Ishizawa, N. Electron density and optical anisotropy in rhombohedral carbonates. III. Synchrotron X-ray studies of CaCO3, MgCO3 and MnCO3. *Acta Crystallographica Section B: Structural Science* **1995**, *51* (6), 929-939.

(8) Landmann, M.; Rauls, E.; Schmidt, W. The electronic structure and optical response of rutile, anatase and brookite TiO2. *Journal of physics: condensed matter* **2012**, *24* (19), 195503.

(9) Ermolaev, G.; Grudinin, D.; Stebunov, Y.; Voronin, K. V.; Kravets, V.; Duan, J.; Mazitov, A.; Tselikov, G.; Bylinkin, A.; Yakubovsky, D. Giant optical anisotropy in transition metal dichalcogenides for next-generation photonics. *Nature communications* **2021**, *12* (1), 854.

(10) Segura, A.; Artús, L.; Cuscó, R.; Taniguchi, T.; Cassabois, G.; Gil, B. Natural optical anisotropy of h-BN: Highest giant birefringence in a bulk crystal through the mid-infrared to ultraviolet range. *Physical Review Materials* **2018**, *2* (2), 024001.

(11) Dou, D.; Wei, C.; Zhang, B.; Yang, D.; Wang, Y. Ultra-High Optical Anisotropy with UV Transmission Achieved by Rational Arrangement of Extended pi-Conjugated Groups. *Angew Chem Int Ed Engl* **2025**, *64* (22), e202504761. DOI: 10.1002/anie.202504761 From NLM PubMed-not-MEDLINE.

(12) Choi, B.; Jo, K.; Rahaman, M.; Alfieri, A.; Lynch, J.; Pribil, G. K.; Koh, H.; Stach, E. A.; Jariwala, D. Giant Optical Anisotropy in 2D Metal-Organic Chalcogenates. *ACS Nano* **2024**, *18* (37), 25489-25498. DOI: 10.1021/acsnano.4c05043 From NLM PubMed-not-MEDLINE.

(13) Mir, S. H.; Nagahara, L. A.; Thundat, T.; Mokarian-Tabari, P.; Furukawa, H.; Khosla, A. Organic-inorganic hybrid functional materials: An integrated platform for applied technologies. *Journal of The Electrochemical Society* **2018**, *165* (8), B3137-B3156.

(14) Niu, S.; Joe, G.; Zhao, H.; Zhou, Y.; Orvis, T.; Huyan, H.; Salman, J.; Mahalingam, K.; Urwin, B.; Wu, J.; et al. Giant optical anisotropy in a quasi-one-dimensional crystal. *Nature Photonics* **2018**, *12* (7), 392-396. DOI: 10.1038/s41566-018-0189-1.

(15) Niu, S.; Milam-Guerrero, J.; Zhou, Y.; Ye, K.; Zhao, B.; Melot, B. C.; Ravichandran, J. Thermal stability study of transition metal perovskite sulfides. *Journal of Materials Research* **2018**, *33* (24), 4135-4143.

(16) Chen, H.; Singh, S.; Mei, H.; Ren, G.; Zhao, B.; Surendran, M.; Wang, Y.-T.; Mishra, R.; Kats, M. A.; Ravichandran, J. Molten flux growth of single crystals of quasi-1D hexagonal chalcogenide BaTiS3. *Journal of Materials Research* **2024**, *39* (13), 1901-1910.

(17) Zhao, B.; Hoque, M. S. B.; Jung, G. Y.; Mei, H.; Singh, S.; Ren, G.; Milich, M.; Zhao, Q.; Wang, N.; Chen, H.; et al. Orientation-Controlled Anisotropy in Single Crystals of Quasi-1D BaTiS3. *Chemistry of Materials* **2022**, *34* (12), 5680-5689. DOI: 10.1021/acs.chemmater.2c01046.

(18) Mei, H.; Ren, G.; Zhao, B.; Salman, J.; Jung, G. Y.; Chen, H.; Singh, S.; Thind, A. S.; Cavin, J.; Hachtel, J. A. Colossal Optical Anisotropy from Atomic‐Scale Modulations. *Advanced Materials* **2023**, *35* (42), 2303588.

(19) Niu, S.; Joe, G.; Zhao, H.; Zhou, Y.; Orvis, T.; Huyan, H.; Salman, J.; Mahalingam, K.; Urwin, B.; Wu, J. Giant optical anisotropy in a quasi-one-dimensional crystal. *Nature Photonics* **2018**, *12* (7), 392-396.

(20) Niu, S.; Zhao, H.; Zhou, Y.; Huyan, H.; Zhao, B.; Wu, J.; Cronin, S. B.; Wang, H.; Ravichandran, J. Mid-wave and long-wave infrared linear dichroism in a hexagonal perovskite chalcogenide. *Chemistry of Materials* **2018**, *30* (15), 4897-4901.

(21) Zhao, B.; Ren, G.; Mei, H.; Wu, V. C.; Singh, S.; Jung, G. Y.; Chen, H.; Giovine, R.; Niu, S.; Thind, A. S. Giant Modulation of Refractive Index from Picoscale Atomic Displacements. *Advanced Materials* **2024**, 2311559.

(22) Wu, J.; Cong, X.; Niu, S.; Liu, F.; Zhao, H.; Du, Z.; Ravichandran, J.; Tan, P. H.; Wang, H. Linear Dichroism Conversion in Quasi-1D Perovskite Chalcogenide. *Advanced Materials* **2019**, *31* (33), 1902118.

(23) zur Loye, H.-C.; Zhao, Q.; Bugaris, D. E.; Chance, W. M. 2H-perovskite related oxides: Synthesis, structures, and predictions. *CrystEngComm* **2012**, *14* (1), 23-39. DOI: 10.1039/c1ce05788j.

(24) Battle, P. D.; Blake, G. R.; Sloan, J.; Vente, J. F. Commensurate and Incommensurate Phases in the SystemA4A′Ir2O9(A=Sr, Ba;A′=Cu, Zn). *Journal of Solid State Chemistry* **1998**, *136* (1), 103-114. DOI: 10.1006/jssc.1997.7666.

(25) Blake, G. R.; Sloan, J.; Vente, J. F.; Battle, P. D. Prediction and Verification of the Structural Chemistry of New One-Dimensional Barium/Copper/Iridium Oxides. *Chemistry of Materials* **1998**, *10* (11), 3536-3547. DOI: 10.1021/cm980317m.

(26) Tranchitella, L. J.; Fettinger, J. C.; Dorhout, P. K.; Van Calcar, P. M.; Eichhorn, B. W. Commensurate columnar composite compounds: Synthesis and structure of Ba15Zr14Se42 and Sr21Ti19Se57. *Journal of the American Chemical Society* **1998**, *120* (30), 7639-7640.

(27) Tilley, R. J. *Perovskites: structure-property relationships*; John Wiley & Sons, 2016.

(28) Darriet, J.; Subramanian, M. A. Structural relationships between compounds based on the stacking of mixed layers related to hexagonal perovskite-type structures. *Journal of Materials Chemistry* **1995**, *5* (4). DOI: 10.1039/jm9950500543.

(29) Gourdon, O.; Petricek, V.; Evain, M. A new structure type in the hexagonal perovskite family; structure determination of the modulated misfit compound Sr9/8TiS3. *Acta Crystallographica Section B: Structural Science* **2000**, *56* (3), 409-418.

(30) Gourdon, O.; Jeanneau, E.; Evain, M.; Jobic, S.; Brec, R.; Koo, H.-J.; Whangbo, M.-H. Influence of the metal–metal sigma bonding on the structures and physical properties of the hexagonal perovskite-type sulfides Sr9/8TiS3, Sr8/7TiS3, and Sr8/7 [Ti6/7Fe1/7] S3. *Journal of Solid State Chemistry* **2001**, *162* (1), 103-112.

(31) Harrison, W. T.; Hegwood, S. L.; Jacobson, A. J. A powder neutron diffraction determination of the structure of Sr 6 Co 5 O 15, formerly described as the low-temperature hexagonal form of SrCoO 3–x. *Journal of the Chemical Society, Chemical Communications* **1995**, (19), 1953-1954.

(32) Boulahya, K.; Parras, M.; González-Calbet, J. The An+ 2BnB′ O3n+ 3 Family (B= B′= Co): Ordered Intergrowth between 2H–BaCoO3 and Ca3Co2O6 Structures. *Journal of solid state chemistry* **1999**, *145* (1), 116-127.

(33) Abraham, F.; Minaud, S.; Renard, C. Preliminary crystal structure of mixed-valency Sr 4 Ni 3 O 9, the actual formula of the so-called Sr 5 Ni 4 O 11. *Journal of Materials Chemistry* **1994**, *4* (11), 1763-1764.

(34) Wang, X.; Li, J.; Shi, Y.; Tsujimoto, Y.; Guo, Y.; Zhang, S.; Matsushita, Y.; Tanaka, M.; Katsuya, Y.; Kobayashi, K. Structure and magnetism of the postlayered perovskite Sr 3 Co 2 O 6: A possible frustrated spin-chain material. *Physical Review B—Condensed Matter and Materials Physics* **2011**, *83* (10), 100410.

(35) Stokes, H. T.; Orden, S. v.; Campbell, B. J. ISOSUBGROUP: an internet tool for generating isotropy subgroups of crystallographic space groups. *Journal of Applied Crystallography* **2016**, *49* (5), 1849-1853.

(36) Gourdon, O.; Cario, L.; Petricek, V.; Perez-Mato, J.; Evain, M. Synthesis, structure determination, and twinning of two new composite compounds in the hexagonal perovskite-like sulfide family: Eu8/7TiS3 and Sr8/7TiS3. *Zeitschrift für Kristallographie-Crystalline Materials* **2001**, *216* (10), 541-555.

(37) Akbarzadeh, A. R.; Ozolins, V.; Wolverton, C. First-principles determination of multicomponent hydride phase diagrams: application to the Li-Mg-NH system. *Advanced Materials (Weinheim)* **2007**, *19*.

(38) Gajdoš, M.; Hummer, K.; Kresse, G.; Furthmüller, J.; Bechstedt, F. Linear optical properties in the projector-augmented wave methodology. *Physical Review B—Condensed Matter and Materials Physics* **2006**, *73* (4), 045112.

(39) Wagner, N.; Seshadri, R.; Rondinelli, J. M. Property control from polyhedral connectivity in ABO 3 oxides. *Physical Review B* **2019**, *100* (6), 064101.

(40) Fadaly, E. M.; Dijkstra, A.; Suckert, J. R.; Ziss, D.; Van Tilburg, M. A.; Mao, C.; Ren, Y.; van Lange, V. T.; Korzun, K.; Kölling, S. Direct-bandgap emission from hexagonal Ge and SiGe alloys. *Nature* **2020**, *580* (7802), 205-209.

(41) Saeki, M.; Onoda, M. Preparation of a new strontium titanium sulfide SrxTiS3 (x= 1.05-1.22) with infinitely adaptive structures. *Journal of Solid State Chemistry* **1993**, *102* (1), 100-105.

(42) Onoda, M.; Saeki, M.; Yamamoto, A.; Kato, K. Structure refinement of the incommensurate composite crystal Sr1. 145TiS3 through the Rietveld analysis process. *Structural Science* **1993**, *49* (6), 929-936.

(43) Pennycook, S.; Jesson, D. High-resolution Z-contrast imaging of crystals. *Ultramicroscopy* **1991**, *37* (1-4), 14-38.

(44) Liu, Y.; Withers, R. L.; Ting, V.; FitzGerald, J. D.; Norén, L. Stacking fault disorder and its diffraction consequences in Ba3MNb2O9 (M= Co and Mn) 1: 2 triple perovskites. *Physica B: Condensed Matter* **2006**, *385*, 564-566.

(45) Mundet, B.; Guzmán, R.; Bartolomé, E.; Lupini, A. R.; Hartman, S.; Mishra, R.; Gázquez, J. An Atomic-Scale Perspective of the Challenging Microstructure of YBa2Cu3O7−x Thin Films. In *Superconductivity: From Materials Science to Practical Applications*, Springer, 2019; pp 189-212.

(46) Tian, W.; Pan, X.; Lee, M.; Eom, C. Microstructure of BaRuO3 thin films grown on (001) SrTiO 3. *Applied Physics Letters* **2000**, *77* (13), 1985-1987.

(47) Wan, C.; Wang, Y.; Norimatsu, W.; Kusunoki, M.; Koumoto, K. Nanoscale stacking faults induced low thermal conductivity in thermoelectric layered metal sulfides. *Applied Physics Letters* **2012**, *100* (10).

(48) Zhao, B.; Mei, H.; Du, Z.; Singh, S.; Chang, T.; Li, J.; Ilyas, B.; Song, Q.; Liu, T. R.; Shao, Y. T. Infrared Optical Anisotropy in Quasi-1D Hexagonal Chalcogenide BaTiSe3. *Advanced Optical Materials* **2024**, *12* (29), 2400327.

(49) Ismail, N.; Kores, C. C.; Geskus, D.; Pollnau, M. Fabry-Pérot resonator: spectral line shapes, generic and related Airy distributions, linewidths, finesses, and performance at low or frequency-dependent reflectivity. *Optics express* **2016**, *24* (15), 16366-16389.

(50) Voronin, A.; Zheltikov, A. The generalized Sellmeier equation for air. *Scientific reports* **2017**, *7* (1), 46111.

(51) Nguyen, L. T.; Cava, R. J. Hexagonal perovskites as quantum materials. *Chemical Reviews* **2020**, *121* (5), 2935-2965.

(52) Blöchl, P. E. Projector augmented-wave method. *Physical review B* **1994**, *50* (24), 17953.

(53) Kresse, G.; Furthmüller, J. Efficiency of ab-initio total energy calculations for metals and semiconductors using a plane-wave basis set. *Computational materials science* **1996**, *6* (1), 15-50.

(54) Kresse, G.; Furthmüller, J. Efficient iterative schemes for ab initio total-energy calculations using a plane-wave basis set. *Physical review B* **1996**, *54* (16), 11169.

(55) Perdew, J. P.; Burke, K.; Ernzerhof, M. Generalized gradient approximation made simple. *Physical review letters* **1996**, *77* (18), 3865.

(56) Dudarev, S. L.; Botton, G. A.; Savrasov, S. Y.; Humphreys, C.; Sutton, A. P. Electron-energy-loss spectra and the structural stability of nickel oxide: An LSDA+ U study. *Physical Review B* **1998**, *57* (3), 1505.

(57) Zunger, A.; Wei, S.-H.; Ferreira, L.; Bernard, J. E. Special quasirandom structures. *Physical review letters* **1990**, *65* (3), 353.

(58) Van de Walle, A.; Tiwary, P.; De Jong, M.; Olmsted, D.; Asta, M.; Dick, A.; Shin, D.; Wang, Y.; Chen, L.-Q.; Liu, Z.-K. Efficient stochastic generation of special quasirandom structures. *Calphad* **2013**, *42*, 13-18.

(59) Allen, L. J.; Findlay, S. Modelling the inelastic scattering of fast electrons. *Ultramicroscopy* **2015**, *151*, 11-22.

For Table of Contents Only